Theoretical investigation of alignment-dependent intense-field fragmentation of acetylene

Katharina Doblhoff-Dier,[1,2,*] Markus Kitzler,[3] and Stefanie Gräfe[2,†]
[1]*Leiden Institute of Chemistry, Leiden University, NL-2333 CC Leiden, Netherlands*
[2]*Institute for Physical Chemistry and Abbe Center of Photonics, Friedrich-Schiller University, D-07743 Jena, Germany*
[3]*Photonics Institute, Vienna University of Technology, 1040 Vienna, Austria*
(Received 25 April 2016; published 6 July 2016)

We analyze the alignment-dependent dissociative and nondissociative ionization of acetylene, C_2H_2. Numerical models describing the yield of the singly and doubly charged ions ($C_2H_2^+$, $C_2H_2^{2+}$) and several fragmentation and isomerization channels ($C_2H^+ + H^+$, $CH^+ + CH^+$, $CH_2^+ + C^+$) as a function of the relative alignment angle between the laser polarization axis and the molecular axis are presented. We apply and compare two different approaches. The first is based on time-dependent density functional theory. The second is a quasi-single-particle approach using the Dyson orbitals. We find good agreement between the results of both methods. A comparison of our theoretical predictions with experimental data allows us to show that the alignment-dependent yield of most reaction channels is described to high accuracy assuming sequential ionization. However, for some of the fragmentation channels, namely, $CH^+ + CH^+$ and $C_2H^+ + H^+$, we find non-negligible influence of recollisional ionization.

DOI: 10.1103/PhysRevA.94.013405

I. INTRODUCTION

Ultrashort and intense infrared laser fields induce strong nonlinear processes in atoms and molecules. Tuning chemical reactions using such laser fields is a promising field of research: For diatoms and small hydrocarbons (e.g., Refs. [1,2]), it has been experimentally demonstrated that reaction control is possible and that different pulse parameters such as the carrier-envelope phase (CEP) and also the relative alignment between the laser polarization direction and the molecular axis allow control of molecular fragmentation. The aim of this paper is to improve the understanding of the alignment dependence of processes that lead to dissociation and that can be exploited in fragmentation control. This necessitates theoretical modeling of the laser-triggered coupled electronic-nuclear dynamics and, thus, processes on a wide range of time scales ranging from the fast electronic response to the molecular vibrational and rotational dynamics.

On the electronic level, the molecular alignment relative to the laser polarization direction has been shown to constitute an important control parameter: The strong-field ionization yield depends on the molecular alignment (e.g., Refs. [3–5]) and within the tunneling regime, the yield has been shown to reflect the orbital structure [3,6–9]. Furthermore, the characteristics of high-order harmonic radiation emitted by molecules depend on the angle between the laser polarization direction and the molecular axis (e.g., Refs. [10–12]). Scanning through different alignment angles has allowed the tomographic reconstruction of molecular orbitals in N_2, CO_2, and other small molecules [13,14].

Since the electronic response depends sensitively on the laser polarization direction, it might be possible to exploit this sensitivity to control molecular reactions with intense, ultrashort pulses. Recently, it has been demonstrated experimentally [15] that reaction control of small molecules is indeed possible by aligning them with respect to the laser polarization direction. In this experiment, acetylene molecules (C_2H_2) were impulsively aligned using a weak pump pulse. A few-cycle infrared probe pulse from a Ti:sapphire laser system with an intensity around 4×10^{14} W/cm^2 was used to induce multiple ionization and fragmentation of the molecules. All fragmentation products were measured in coincidence. The relative yields of several reaction channels, namely, ionization to $C_2H_2^+$ and $C_2H_2^{2+}$ and fragmentation into $C_2H^+ + H^+$, $CH^+ + CH^+$, and $CH_2^+ + C^+$, where shown to depend on the delay time between the alignment pulse and the probe pulse. Due to the rotational wave-packet motion, this corresponds to different alignments of the molecules.

In this paper we provide a detailed theoretical analysis of these experimental results. The models discussed in this paper provide an interpretation and a deeper understanding of the fundamental physical processes determining the control.

We start our discussion with a comprehensive analysis of the electronic potential landscape of acetylene. This will allow an investigation of the possible nuclear rearrangement channels and allows one to relate specific nuclear fragmentation reactions to the population of specific electronic states. The dynamic response of electrons and nuclei to the laser field and their alignment dependence is discussed in Secs. III A and III B. In Sec. IV, the results from the theoretical analysis are compared to the experimental values, providing further insight into the reaction mechanisms.

II. QUANTUM CHEMICAL CALCULATIONS ON ACETYLENE

A. Potential landscape of acetylene

We have calculated selected cuts through acetylene's potential landscape using the program package MOLCAS [16]. We use the information derived from the potential energy surfaces to discuss which states allow fragmentation reactions and which support the formation of nonfragmenting ions and dications.

*k.doblhoff-dier@umail.leidenuniv.nl
†s.graefe@uni-jena.de

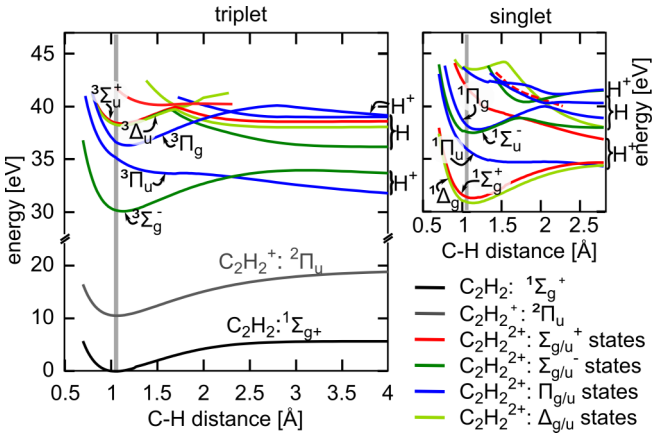

FIG. 1. The C-H stretching mode of linear acetylene. Dicationic states, SA-CAS(8,9) [SA-CAS(8,10) for Π states]; neutral and cationic states, CAS(8,8). Basis set: aug-cc-pVTZ. C-C = 1.2 Å, other C-H = 1.06 Å. The symbols H^+ and H denote dissociation into $C_2H^+ + H^+$ and $C_2H^{2+} + H$, respectively. The gray bar indicates the Franck-Condon region. Dashed lines indicate regions of state crossings with higher excited states.

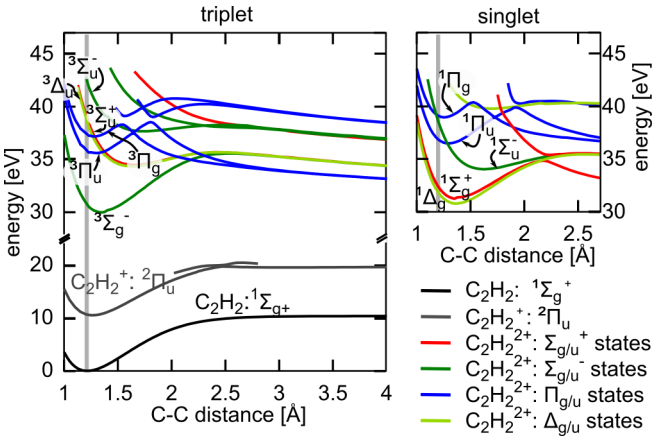

FIG. 2. Same as Fig. 1 but for the C-C stretching mode [SA-CAS(8,8), C-H = 1.06 Å].

Figures 1 and 2 show the results along the C-H and the C-C stretching modes of acetylene in the neutral, the ionic, and the dicationic manifold.[1] The calculations were performed using a state-averaged complete active space approach with m electrons in n active orbitals [SA-CAS(m,n)] as given in the figure captions. The calculations were performed in the C_{2v} subgroup. The state average was performed over all states belonging to one irreducible representation. The present calculations are in agreement with values available in the literature [17–21].

In the cationic manifold, the electronic ground state is bound. In the dication, the triplet ground state ($^3\Sigma_g^-$) and the first two singlet states are metastable, featuring a high barrier to dissociation (see Figs. 1 and 2). This is consistent with experimental observations in which $C_2H_2^{2+}$ is found to be metastable with lifetimes of $C_2H_2^{2+}$ of more than 1 μs [21].

The next higher excited states, the $^3\Pi_u$ and $^1\Pi_u$ states, have vertical excitation energies relative to the $^3\Sigma_g^-$ ground electronic state of 5.5 and 6.3 eV, respectively.[2] These states are strongly dissociative along the C-H stretching mode, as can be seen in Fig. 1. From a Mulliken charge analysis, we could deduce that the Π_u states dissociate into the $C_2H^+ + H^+$ and not into the $C_2H^{2+} + H$ channel, as indicated by the "H^+" symbol in Fig. 1. Along the C-C stretching mode (Fig. 2), the $^3\Pi_u$ and the $^1\Pi_u$ states both show a potential barrier to dissociation. However, we have confirmed by reduced dimensional nonadiabatic dynamics calculations that dissociation into $CH^+ + CH^+$ is possible from these low-lying excited states. This is also in agreement with experimental results [2]. The $^3\Pi_u$ state is also known to have a pathway to isomerization with energetically low-lying transition states [22].

B. Ionization pathways and Dyson orbitals

Next, we address the question of how the different states in the ionic and dicationic manifolds can be populated. Figure 3 shows the seven energetically lowest-lying molecular orbitals of acetylene, calculated near the equilibrium geometry of C_2H_2 using a CAS(8,8) calculation and the cc-pVTZ basis set.

The ground-state configuration of C_2H_2 is dominated by the following determinant of molecular orbitals: $(1\sigma_g^2, 1\sigma_u^2, 2\sigma_g^2, 2\sigma_u^2, 3\sigma_g^2, 1\pi_u^4)$, where the orbitals are labeled according to their symmetries and ordered according to increasing pseudo-single-particle energies. The exponents denote the orbital population. This configuration corresponds to the double occupation of all orbitals shown in Fig. 3. The highest occupied molecular orbital is the doubly degenerate $1\pi_u$ orbital, resulting mainly from the bonding superposition of the carbon p orbitals lying orthogonal to the molecular axis. The next-lower-lying orbitals, the $3\sigma_g$, the $2\sigma_u$, and the $2\sigma_g$ orbitals, describe bonding and antibonding superpositions of the carbon sp orbitals and the hydrogen $2s$ orbitals. The $1\sigma_g$ and $1\sigma_u$ orbitals are formed from the carbon $1s$ orbitals and are energetically well separated from the other orbitals and remain doubly occupied for all electronic states considered.

The cationic ground state, $^2\Pi_u$, mainly corresponds to a configuration in which one electron is missing from the π_u

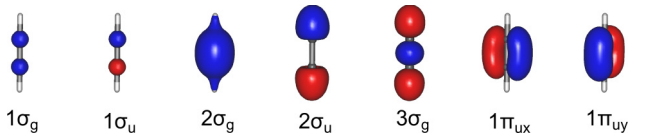

FIG. 3. Molecular orbitals of C_2H_2 with near double occupancy in the neutral ground state, calculated in GAMESS using a CAS(10,10), aug-cc-pVTZ basis (isovalue 0.1).

[1]The nomenclature of states follows the nomenclature in the linear, symmetric ground-state geometry.

[2]Note that other than for Figs. 1 and 2, where different symmetry groups were used to facilitate the calculation of highly excited states, the excitation energies stated were calculated without symmetry in order to obtain more exact relative energies between states, which would fall into different symmetry representations in C_{2v} [method, SA-CAS(8,10); basis set, aug-cc-pVTZ].

TABLE I. Occupation of orbitals in configuration state functions (CSFs) contributing with weights larger than 0.04 for the lowest-lying dicationic states.

	CSF					
State	$2\sigma_g$	$2\sigma_u$	$3\sigma_g$	$1\pi_u^x$	$1\pi_u^y$	Weight
			Dication			
$^3\Sigma_g^-$	↑↓	↑↓	↑↓	↑	↑	0.96
$^1\Delta_g$ (1)	↑↓	↑↓	↑↓	↑	↓	0.85
	↑↓	↑↓	↑↓	↑↓		0.05
	↑↓	↑↓	↑↓		↑↓	0.05
$^1\Delta_g$ (2)	↑↓	↑↓	↑↓	↑↓		0.43
	↑↓	↑↓	↑↓		↑↓	0.43
$^1\Sigma_g^+$	↑↓	↑↓	↑↓	↑↓		0.47
	↑↓	↑↓	↑↓		↑↓	0.47
$^3\Pi_u$ (1)	↑↓	↑↓	↑	↑↓	↑	0.89
$^3\Pi_u$ (2)	↑↓	↑↓	↑	↑	↑↓	0.89
$^1\Pi_u$ (1)	↑↓	↑↓	↑	↓	↑↓	0.91
$^1\Pi_u$ (2)	↑↓	↑↓	↑	↑↓	↓	0.91

orbital, while one electron is missing from the $3\sigma_g$ electron in the cationic excited $^2\Sigma_g$ state.

The main configurations for the lowest-lying dicationic states are shown in Table I.

The lowest-lying dicationic, metastable $^3\Sigma_g^-$, $^1\Delta_g$, and $^1\Sigma_g^+$ states are dominated by configurations in which two electrons are missing from the π_u orbitals. The lowest-lying dissociative, dicationic states, the Π_u states, correspond to configurations with one electron missing from the π_u and one missing from the lower-lying $3\sigma_g$ orbital. The dissociative Π_u states can thus either be populated by ionization from the highest occupied orbitals (the π_u orbitals) and subsequent excitation or directly via ionization from the lower-lying orbitals as shown schematically in Fig. 4. This is reflected by the shape of the Dyson orbitals, which are defined as

$$\phi_D(\mathbf{r}) = \langle \Psi^{N-1}(\mathbf{r}_1, \ldots, \mathbf{r}_{N-1}) | \Psi^N(\mathbf{r}_1, \ldots, \mathbf{r}_{N-1}, \mathbf{r}) \rangle_{\mathbf{r}_1, \ldots, \mathbf{r}_{N-1}}. \quad (1)$$

These are shown in Fig. 5 for the overlap of the 12-electron wave function of the dicationic states with the 13-electron wave function of the cationic ground state. The Dyson orbital is of

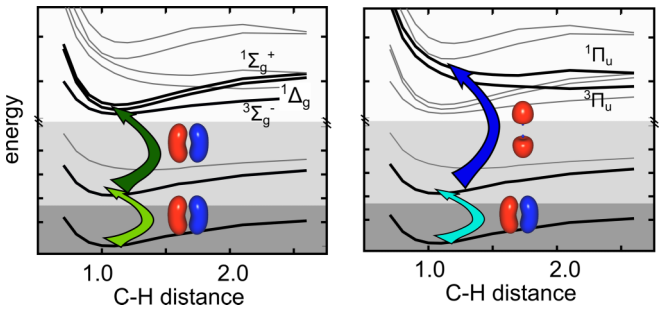

FIG. 4. Schematic drawing of states populated after the extraction of two π_u electrons (left) and one σ_g and one π_u electron (right). Dark gray region, neutral; light gray region, cationic states; all other states, dicationic states.

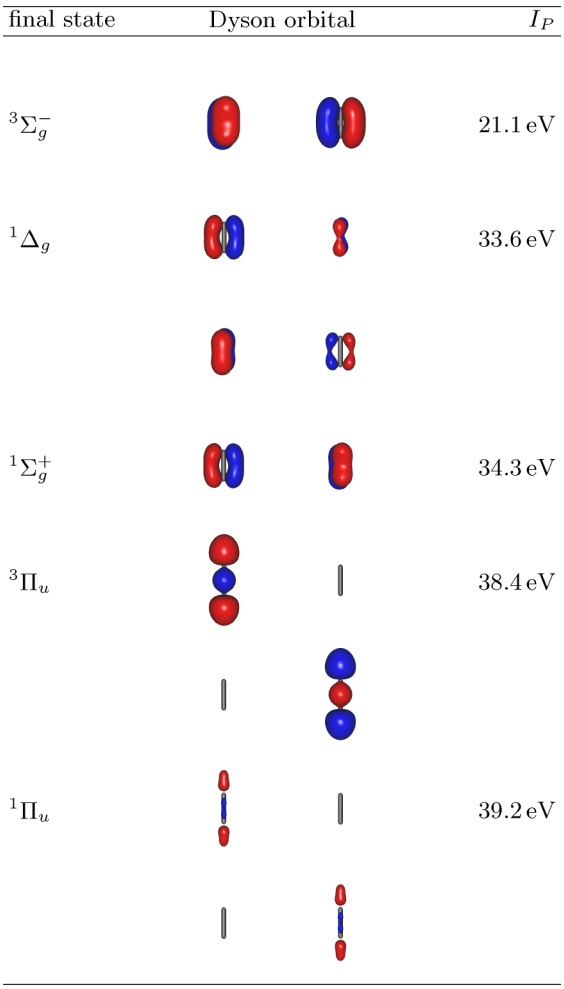

FIG. 5. Dyson orbitals from the degenerate $^2\Pi_u$ state to different dicationic states. The left- and right-hand figures show Dyson orbitals for the two different orientations of the degenerate $^2\Pi_g$ state. For degenerate final states, the Dyson orbitals for the different orientations are given in subsequent rows. Method, CAS(8,8); basis, adjusted aug-cc-pV5Z basis (see text for details). Note that the orientation of the degenerate states is not necessarily the same for different states.

π_u type for the lowest three states and of σ_g-type orbital for the dissociative Π_u states, indicating that direct electron removal from these orbitals can lead to the population of these states. Although ionization from the π_u orbitals may be expected to be strongest, strong-field ionization from lower-lying orbitals has been observed to play an important role for several molecules (e.g., Refs. [7,23–25]), particularly when considering different alignment angles.

III. NUMERICAL SIMULATION

The simultaneous description of all degrees of freedom relevant to describe the experiment [15], the rotational and vibrational nuclear and the electronic degrees of freedom, is so far computationally unachievable. However, the dynamics proceed on different time scales: the slowest dynamics, the rotational motion of the molecule, proceeds on the picosecond time scale, while the vibrational motion takes place on the femtosecond time scale. Ionization is expected to occur on a

subcycle time scale. Additionally, the probe pulse is very short (5 fs) and tunneling ionization depends nonlinearly on the pulse intensity. This limits ionization and excitation to time scales that can in first approximation be considered to be shorter than the time it takes for significant nuclear rearrangement to take place. This approximation allows separating the nuclear and the electronic processes, as is commonly done, and to meet the computational challenge by breaking the full process into several subprocesses occurring on different time scales.

A. Alignment-dependent ionization

In the last section, we established a connection between the ionization from π_u orbitals and the population of nondissociative states, leading to the formation of $C_2H_2^+$ and $C_2H_2^{2+}$. The ionization from the σ_g orbital was connected with the population of dissociative dicationic states leading to the formation of $C_2H^+ + H^+$, $CH^+ + CH^+$, and $CH_2^+ + C^+$. Based on this information, we now build a model for the alignment-dependent fragmentation of acetylene depending solely on the alignment-dependent ionization from different orbitals. Field excitation processes are treated separately in Sec. V B.

Double ionization may proceed sequentially and nonsequentially: While the first ionization step is necessarily field induced, the second ionization step may be either field driven or caused by electron recollision [26,27]. Due to the comparatively high intensity of the probe pulse used in the experiment [15], one may expect ionization to occur predominantly sequentially: Experimentally, it has been shown that for 50-fs pulses, sequential ionization becomes dominant over recollisional ionization for intensities above approximately $2 \times 10^{14}\,\mathrm{W/cm^2}$ [28]. We therefore model ionization sequentially. We address the possibility of nonsequential ionization at a later point in this paper.

In the present model, we assume that the first and second ionization steps take place independently of each other. Furthermore, we assume that the molecule's nuclear arrangement does not change during the ionization process. This is a legitimate approximation as the ionization will dominantly take place during the central field cycle of the very short laser pulse (5 fs), due to the exponential dependence of the ionization rate on the field strength [29–34].

However, even if the nuclear motion is neglected, one would still have to describe the strong-field dynamics of all electrons in the molecule. For the 14 electrons present in acetylene, an exact numerical treatment is not feasible at present. To circumvent this problem, two different approaches were used: (a) an approach based on time-dependent density functional theory (TD-DFT) and time-dependent Kohn-Sham orbitals and (b) an effective one-electron approach based on the Dyson orbital and the assumption of strong-field ionization via tunneling.

1. Description via TD-DFT

In the present simulation, the TD-DFT calculations were performed using the OCTOPUS code [35–37] on a grid with complex absorbing boundaries using the local-spin-density approximation (LSDA) exchange functional and a modified local-density approximation (LDA) correlation functional by Perdew and Wang [38] available in the standard OCTOPUS distribution.

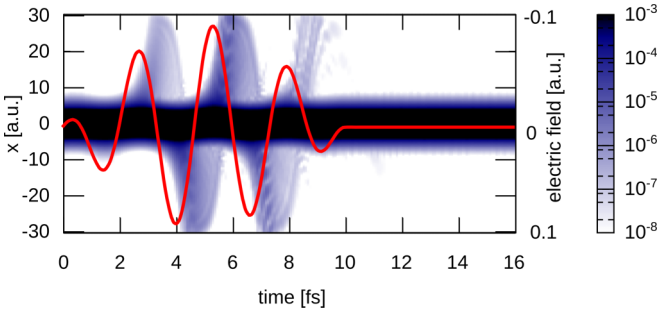

FIG. 6. Time evolution of the electronic density of $C_2H_2^+$ projected onto the laser polarization direction for an alignment angle of $\theta = 40^\circ$ when starting from the electronic ground state. Nuclear coordinates are fixed. Superimposed red line, laser electric field.

The TD-DFT approach has the advantage of including, to a certain extent, many-electron effects and thus simultaneous excitation and ionization in the presence of an intense laser field, while substantially reducing the numerical effort, since only the three spatial dimensions of the density are considered. On the other hand, DFT is not exact and LSDA is known to have problems describing total ionization yields [39,40] due to the incorrect description of the Coulomb tail (the potential decreases exponentially, instead of as $1/r$). In the present application, we are, however, not interested in the total ionization yield but only in its alignment dependence, which is expected to be influenced by the orbital shape [3,6–9]. A potentially better description of the exchange correlation can be obtained, for example, by using the generalized gradient approximated exchange-correlation potential by Leeuwen and Baerdens [39,41], which has the correct asymptotic behavior. This is, however, not only numerically more expensive; the calculation also suffers from numerical instabilities on a large grid. Several independent calculations suggest that, qualitatively, the alignment dependence is not influenced by the choice of the exchange-correlation functional. We therefore use LSDA in the following calculations.

In the simulations, the box size was set to at least $64 \times 40 \times 37$ a.u., where the first dimension corresponds to the laser polarization direction and defines, together with the second dimension, the plane in which the molecular axis lies. This box is sufficiently large to easily accommodate the classical tunnel exit. A $\sin^2$-shaped imaginary potential was applied to avoid reflections from the grid ends: the width of the imaginary absorbing boundaries was 4 a.u., and the absolute value of their height was 1.5 a.u.

A strong and short laser pulse [4.5 fs full width at half maximum (FWHM) with a sinusoidal envelope, $I = 2.8 \times 10^{14}\,\mathrm{W/cm^2}$], linearly polarized at an angle θ relative to the molecular axis, was applied to the neutral and ionic molecule.[3]

[3]To limit the amount of double ionization and the space charge in the continuum, the laser intensity in the simulations was chosen slightly lower than in the experiment. At the intensity used, the total amount of charge lost is lower than 0.6 a.u. for C_2H_2, 0.1 a.u. for $C_2H_2^+$ in the ground state, and 0.2 a.u. in the excited state.

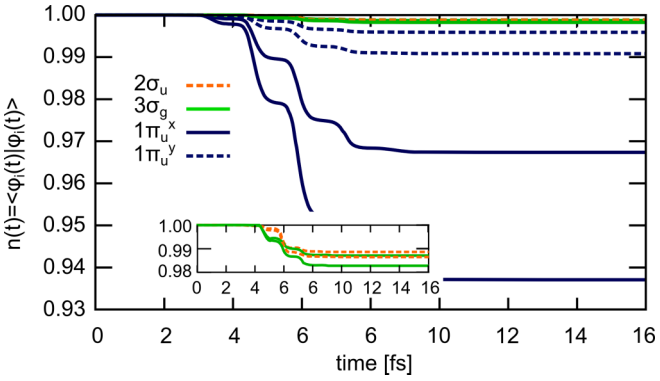

FIG. 7. Time evolution of $n_i(t;40^\circ)$ of the Kohn-Sham spin orbitals of $C_2H_2^+$ starting from the electronic ground state. Nuclear coordinates are fixed; laser field is as in Fig. 6. Lines with the same color (shade of gray) correspond to spin-up and spin-down orbitals whose contributions are added in the model.

The ionic molecule was thereby considered both in its ground state and in an excited state, which was assumed to correspond to a configuration with one electron missing from a $3\sigma_g$ Kohn-Sham orbital.

Near each field maximum, electronic density is drawn away from the molecule as shown in Fig. 6.

The charge lost during the calculation via the absorbing boundaries is interpreted as the probability for single ionization at the angle θ.

By monitoring the decrease in the norm as a function of the alignment angle θ, the angular dependence of the total ionization yield can be evaluated. To evaluate the probability to populate a certain state via ionization additional assumptions are made: Based on the analysis in Sec. II A, it is clear that the probability to populate the states of interest is strongly connected with the probability to ionize from a π_u-type molecular orbital and/or from a σ_g-type orbital. Since we have verified that the Kohn-Sham orbitals are similar to the molecular orbitals, one may connect the decrease of the norm of those orbitals with the population of either the ground or the excited dissociative states.

Figure 7 displays the time evolution of the charge contained in each Kohn-Sham orbital φ_i. The charge is thereby calculated as follows:

$$n_i(t;\theta) = N_i^o \langle \varphi_i(t;\theta) | \varphi_i(t;\theta) \rangle, \tag{2}$$

where N_i^o is the the initial occupation number of the ith orbital.[4]

Due to the strong mixing of the Kohn-Sham orbitals in the laser field, a direct mapping of the charge lost from different Kohn-Sham orbitals to the probability to populate a specific final state by ionization during the interaction with the IR field is not possible.

As shown in Fig. 8(a), especially the coupling between the $3\sigma_g$ and $2\sigma_u$ orbitals is very large. The character of these two orbitals effectively switches ($\langle \varphi_{3\sigma_g} | \varphi_{2\sigma_u} \rangle \approx 1$) at certain times

[4]The calculation of this value was implemented by the authors in a private version of the OCTOPUS code.

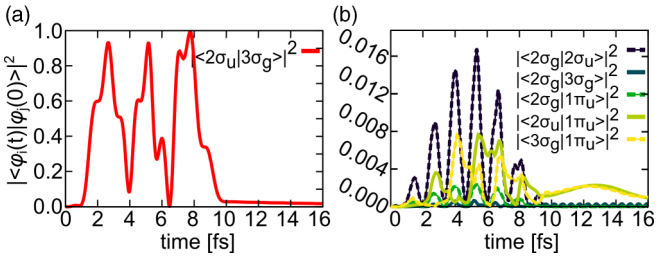

FIG. 8. Time evolution of selected projections $P_{i,j} = |\langle \varphi_i(t) | \varphi_j(0) \rangle|^2$ for an alignment angle of $\theta = 40^\circ$. Left: $P_{2\sigma_u,3\sigma_g}$. Right: couplings between π_u and $\sigma_{u/g}$ states and couplings between lower-lying σ states.

during the propagation. Couplings to lower-lying σ states, on the other hand, are negligible [see Fig. 8(b)] and the coupling between the π_u and the σ states remains well below 1.5% even for $\theta = 90^\circ$, where the strongest coupling can be expected due to symmetry considerations.

Because of the strong coupling of the $2\sigma_u$ and $3\sigma_g$ orbitals, norm lost from the orbital initially corresponding to the $2\sigma_u$ orbital partially contains norm lost from the orbital with $3\sigma_g$ character. Hence, one cannot discern ionization from these two orbitals. Ionization from σ_g and σ_u orbitals was thus treated as a sum over all σ orbitals. Due to the weak coupling of the π states to the σ states, it is a reasonably good approximation to separate the ionization from σ-type orbitals and π-type orbitals. The ionization probabilities from σ and π orbitals can thus be defined as follows:

$$p_\sigma^{+/2+}(\theta) = \sum_{i=\sigma \text{ orb}} \left[n_i^{0/+}(t=0,\theta) - n_i^{0/+}(t=t_f,\theta) \right], \tag{3}$$

$$p_\pi^{+/2+}(\theta) = \sum_{i=\pi \text{ orb}} \left[n_i^{0/+}(t=0,\theta) - n_i^{0/+}(t=t_f,\theta) \right], \tag{4}$$

where θ denotes the angle between the laser polarization direction and the molecular axis. The time t_f is chosen sufficiently long after the end of the pulse such that the electronic density released during the pulse has left the grid. The superscripts "+" and "2+" of p denote ionization to $C_2H_2^+$ and $C_2H_2^{2+}$, respectively, while the superscripts "0" and "+" of the n_i denote the orbital charges in the neutral molecule and the ion.

While the mixing of fully occupied orbitals in TD-DFT is an artifact and seems unfavorable for the present analysis, it should be kept in mind that this coupling can reflect physically relevant processes as soon as the norm is lost from one of the orbitals. Then, a "real" coupling between the orbitals becomes possible and can be related to relevant observables: The mixing of the σ_g and σ_u orbitals leads to the formation of asymmetric orbitals due to the opposite symmetry of the σ_g and σ_u orbitals. Ionization from the time-dependent orbital can thus be expected to lead to charge localization during fragmentation. Such a charge localization has indeed been observed by Alnaser *et al.* [42] as a function of the carrier-envelope phase.

The total ionization probabilities, $p_i(\theta)$ [Eqs. (3) and (4)] are displayed in Fig. 9. The π orbitals ionize preferentially when aligned orthogonally to the laser polarization axis, while the σ orbitals feature preferential ionization at parallel

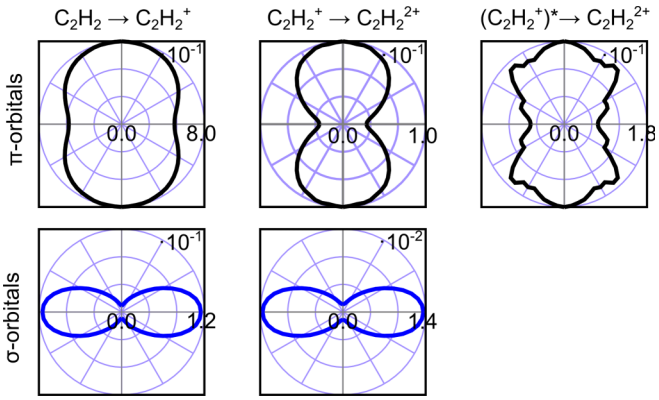

FIG. 9. Angular plots of the alignment-dependent ionization probabilities from specific orbitals. Top row, black lines: probability to ionize from a π orbital; bottom row, blue lines: probability to ionize from a σ orbital for (a) C_2H_2, (b) $C_2H_2^+$, and (c) $C_2H_2^+$*.

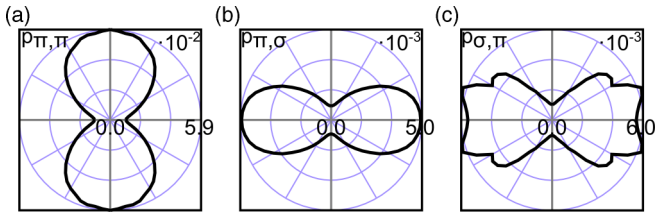

FIG. 10. Angular plots of the alignment-dependent probability for sequential double ionization. (a) Ionization from a π orbital in the first and second ionization step, $p^{2+}_{\pi,\pi}$; (b) ionization from a π orbital in the first step and from a σ orbital in the second step, $p^{2+}_{\pi,\sigma}$; and (c) ionization from a σ orbital followed by ionization from a π orbital, $p^{2+}_{\sigma,\pi}$. See text for details.

alignment. Since strong-field ionization has been found to reflect the orbital shape [3,6–9], this behavior agrees with the qualitative expectations based on the different orbital shapes. Ionization from π orbitals in C_2H_2 [Fig. 9(a)] depends only rather weakly on the alignment. This may be explained by the fact that in the neutral molecule, ionization from the π orbital is estimated to proceed in the over-the-barrier regime: For an atomic potential at $I = 4 \times 10^{14}\,\mathrm{W/cm^2}$, the barrier maximum lies at -16 eV with respect to the ionization continuum. The ionization potential I_P from the π orbitals, corresponding to ionization to the cationic ground state, is given by $-I_P \approx -11.6$ eV [43]. This energy is clearly higher than the barrier maximum.

For both the first and the second ionization step, the alignment dependence is observed to be more pronounced for the σ-type orbitals than for the π-type orbitals. This is attributed to a combined effect of the lower ionization potential for the π_u orbitals and the shape of the orbitals.

Having determined the angular dependence of the single ionization yield, we calculate double ionization yields by assuming that sequential ionization is the dominant mechanism. Assuming that the two ionization steps are independent of each other and neglecting interference effects, the double ionization yields are defined as

$$p^{2+}_{a,b}(\theta) = \int_0^{t_f} \left(\sum_a n_i^0(0,\theta) - n_i^0(t,\theta) \right) \times \left(\sum_b n_i^+(t,\theta) - n_i^+(t_f,\theta) \right) dt, \qquad (5)$$

with $a,b = \pi,\sigma$. The probability $p^{2+}_{\pi,\sigma}$ denotes ionization from a π-type orbital in the first step and from a σ-type orbital in the second step, etc. If the first ionization step corresponds to ionization from a σ-type orbital, the charge evolution n_i^+ from the calculations for the excited ion should be used in the above expression. The resulting double ionization probabilities are shown in Fig. 10.

Due to the stronger alignment dependence of the ionization from the σ orbitals, the combined probability for ionization from a π-type orbital followed by a σ-type orbital and vice versa is dominated by the angle dependence of the σ orbital; i.e., it is larger for small angles θ [see Figs. 10(b) and 10(c)], while $p^{2+}_{\pi,\pi}$ is larger for orthogonal alignment.

As described in Sec. II A, the probability p_π^+ can be assumed to correspond to the probability to populate the nondissociative singly ionic ground state $^2\Pi_u$, $p^{2+}_{\pi,\pi}$ to populating a nondissociative dicationic state ($^3\Sigma_g^-$, $^1\Delta$, $^1\Sigma_g^+$) and $p^{2+}_{\pi,\sigma}$ and $p^{2+}_{\sigma,\pi}$ to populating an excited dissociative dicationic state ($^3\Pi_u$, $^1\Pi_u$). The norm losses obtained via TD-DFT, which are strongly alignment dependent for the σ orbitals and—less so—for the π orbitals, can thus be related to an alignment-dependent fragmentation yield.

2. Description via Dyson orbitals and tunneling

The TD-DFT results presented in the last section feature alignment-dependent probabilities for sequential ionization. However, very often, the results of TD-DFT are to be taken with caution when used to describe ionization processes. Thus, in this section, we present a conceptually completely different approach based on different approximations: The TD-DFT results presented in the last section are compared to results from an ansatz based on Dyson orbitals, as described in the following.

The Dyson orbital approach used in the present paper is based on the method described in Ref. [44] using the eikonal approximation with a first-order correction for a single center potential [45]. In this approach, ionization is treated as a tunneling process from an effective one-electron system described by the Dyson orbital [see Eq. (1)] via the ionization rate [44,45]

$$\Gamma \propto \iint \sqrt{2I_p} \left[\left(\frac{4I_P}{E z_0} \right)^{\frac{Q+1}{\sqrt{2I_p}}} e^{-\frac{\sqrt{2I_p}^3}{3E} + \sqrt{2I_p} z_0} \right]^2 \times |\tilde{\phi}_D(p_x,p_y,z_0)|^2 e^{-p_\perp^2 \frac{\sqrt{2I_p}}{E}}\, dp_x\, dp_y, \qquad (6)$$

where the z axis corresponds to the laser polarization axis with laser field strength E. $\tilde{\phi}_D(p_x,p_y,z_0)$ is the two-dimensional Fourier transform of the Dyson orbital in the plane orthogonal to the laser polarization at z_0, $\tilde{\phi}_D(p_x,p_y,z_0) = \mathcal{F}\{\phi_D(x,y,z_0)\}_{x,y}$, which has been calculated numerically on a grid. In this expression, $p_\perp = \sqrt{p_x^2 + p_y^2}$ and I_P denotes the ionization potential. Q is the charge of the molecule prior to ionization. The value of z_0 should be chosen to lie

within the potential barrier, thus setting an upper limit to the field strength: Too-high field strengths would narrow the border too much or render a description impossible in the case of over-the-barrier ionization. For moderate field strengths, the exact value of z_0 should not influence the final results [44,45]. Although not clearly visible in Eq. (6), the first three terms in square brackets arise from the eikonal approximation with a first-order correction for a single center potential of $e^{\int_{z_0}^{z_{ex}} p_z(z')dz'}$. In Eq. (6), it is thus tacitly assumed that the exit of the barrier, z_{ex}, can be calculated assuming a single center potential. The further z_{ex} lies from the center of the molecule, the better this approximation will be.

This Dyson approach is based on the formation of a quasistatic barrier. Since the first ionization step for the parameters investigated here proceeds classically over the barrier, the tunneling model is only applicable to the second ionization step. Applying the model at the experimentally used intensity (4×10^{14} W/cm^2) is, however, problematic due to the single center approximation made in Eq. (6): At $I = 1.2 \times 10^{14}$ W/cm^2, the barrier entrance z_{in} for $I_P = 21$ eV (ionization to the $^3\Sigma_g$ state; see Fig. 5) is given by $z_{in} = 3$ a.u. when assuming a single center potential. The barrier exit z_{ex} is given by $z_{ex} = 11$ a.u. in this case. Due to the spatial extent of the molecule of about 3 a.u., the true tunnel entrance will be shifted to larger values compared to these predictions for a single center potential. At higher intensities, the tunnel exit moves closer to the tunnel entrance and z_0 cannot be safely chosen within the true barrier any more. We thus limit our analysis to an intensity range of 8.8×10^{13} to 1.2×10^{14} W/cm^2. Within this intensity range, no strong changes in the alignment dependence of the ionization yield were observed. In the comparison with the TD-DFT results, the results for $I = 1.2 \times 10^{14}$ W/cm^2 are used. For this intensity, values of z_0 ranging from 6 to 7 a.u. were compared and yielded consistent results. Since the Dyson orbital ϕ_D is sampled at a distance z_0 from the molecular center, larger values of z_0 were not considered due to the limited size of the basis set representing the wave function and the quality of the wave function at very large distances. The results presented in the following were obtained at $z_0 = 6.5$ a.u.

The wave functions and ionization potentials defining the Dyson orbital were calculated using MOLCAS [16] using CASPT2 with an active space containing nine active electrons in eight orbitals. Since the method requires a very good description of the wave-function tails at several atomic units from the molecular center, a modified aug-cc-pV5Z basis was used to calculate the wave functions. To allow a high-quality description of the tails, two additional diffuse orbitals for each angular momentum were added to the aug-cc-pV5Z basis. On the other hand, the orbitals with angular momentum quantum number $l = 5$ (h orbitals) were removed from the basis to limit the size of the basis set. The molecular geometry was kept at the ground-state geometry of the neutral molecule, i.e., linear with a C-C bond distance of 1.2 Å and a C-H bond distance of 1.0 Å, similarly to the TD-DFT calculations. The Dyson orbitals were calculated from the resulting wave functions via Eq. (1) and are shown in Fig. 5. The ionization potential I_P, which enters the ionization rate given by Eq. (6), was calculated from the energy difference of the $(N-1)$-particle and the N-particle states.

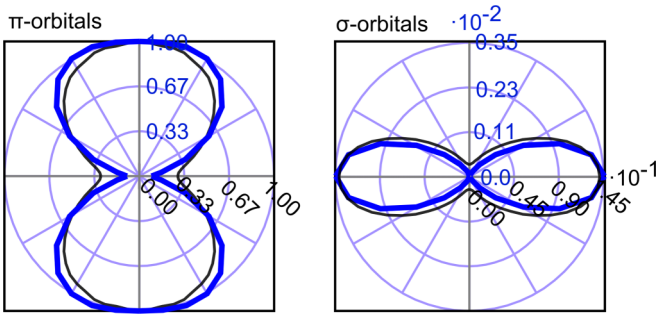

FIG. 11. Comparison of the ionization probability from $C_2H_2^+$ to $C_2H_2^{2+}$ calculated via TD-DFT (thin black line, black scale on x axis) and the ionization rate calculated via the Dyson orbital approach (thick blue line, blue scale on y axis). Left: for π-type orbitals; right: for σ-type orbitals. Arbitrary units are used in all cases.

To allow a comparison with the TD-DFT results discussed in the last section, the ionization rates for the π-type Dyson orbitals corresponding to ionization to the $^3\Sigma_g^-$, $^1\Delta_g$, and $^1\Sigma_g^+$ states were added, as were the rates for σ-type Dyson orbitals for ionization to the $^3\Pi_u$ and $^1\Pi_u$ states. Figure 11 shows a comparison of the alignment-dependent ionization probability computed via TD-DFT with the ionization rate calculated using the Dyson-orbital approach.

Overall, Fig. 11 shows a very good agreement between the TD-DFT results and the Dyson-orbital calculations. The differing relative ionization probability from the π and σ orbitals in the two approaches can be attributed to the different intensities used in the two calculations. Within the intensity range accessible in the Dyson orbital approach (8.8×10^{13} to 1.2×10^{14} W/cm^2), the relative importance of ionization from the σ orbitals strongly increases for increasing intensity, which is consistent with the comparatively high influence of ionization from σ orbitals observed in the TD-DFT approach at $I = 2.8 \times 10^{14}$ w/cm^2. The alignment dependence did not change considerably with intensity in the Dyson orbital approach. The overall slightly more pronounced alignment dependence in the Dyson orbital approach can be explained by the very different approximations made in the two approximations. While TD-DFT suffers from deficiencies in the description of the exchange correlation and the long-range interaction, the Dyson approach necessitates tunneling and is based on a single-active-electron picture. The single-active-electron approximation neglects electronic coupling and excitation, which was observed to play an important role in the TD-DFT approach. Nevertheless, the excellent agreement between the TD-DFT approach and the Dyson-orbital approach strongly suggests the reliability of both approaches, the Dyson orbital and the TD-DFT approach.

B. Rotational wave packet

We describe the molecular rotational dynamics following impulsive alignment within the rigid rotor approximation. Electronic excitations are assumed to be negligible due to the off-resonance nature of the laser field and the low intensity of the alignment pulse. Therefore, the interaction of the laser pulse with the molecule can be described via the polarizability

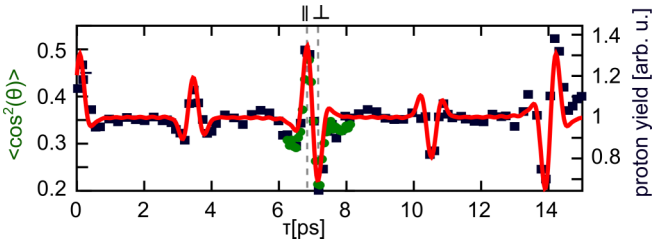

FIG. 12. Red (gray) continuous line, simulation of $\langle\cos^2(\theta)\rangle$; green (light gray) dots, experimentally measured expectation value of $\cos^2(\theta)$ derived from the Coulomb explosion data of $C_2H_2^{4+}$ [15]; blue (dark gray) squares, proton yield as a function of the delay time τ. The symbols ∥ and ⊥ mark the delay times τ with highest probability to find the molecule aligned parallel and perpendicular to the laser polarization direction.

tensor and the rotational constant B as described in Ref. [46]. Values for the polarizability and for B were taken from the literature with a polarizability orthogonal to the molecular axis of 2.7 Å^3, an anisotropy of 1.8 Å^3 [47], and a rotational constant of $B = 1.18\,\mathrm{cm}^{-1}$ [48]. A Boltzmann distribution $p(J_s,M_s) = p(J_s)/(2J_s+1)$ is assumed as initial, incoherent population of different rotational states with quantum numbers J_s and M_s. The initial rotational temperature was set to 100 K, equal to the value estimated from the experiment [15]. Nuclear spin statistics were taken into account by assuming a ratio of 3:1 between the population of states with odd and even rotational quantum numbers to account for the fermionic character of the hydrogen atoms. The intensity of the alignment pulse was set to $2.4\times10^{13}\,\mathrm{W/cm^2}$ and the full width at half maximum of the field to 50 fs similarly to the experimental values. Since the duration of the alignment pulse is short compared to the rotational period of acetylene, the interaction with the pump pulse leads to a coherent population $w_f(J_s,M_s,J)$ of higher and lower rotational states with quantum number J and thus to the creation of a rotational wave packet evolving in time. Rotational states up to a maximum quantum number of $J = 20$ were taken into account to obtain convergence in the final results.

The probability to find a molecule at a delay τ at an angle θ relative to the laser polarization direction is given by

$$f(\theta,\tau) = \sum_{J_s,M_s} 2\pi\sin\theta\frac{p(J_s)}{2J_s+1} \times\left|\sum_J e^{-i\frac{B}{\hbar}J(J+1)\tau} w_f(J_s,M_s,J)Y_{J,M_s}(\theta)\right|^2. \quad (7)$$

This probability distribution plays a central role in the semiclassical model below.

Figure 12 shows a comparison of the simulated [46] and measured [15] value of $\langle\cos^2\theta\rangle$ as a function of delay time τ to the alignment pulse. As can be seen, the degree of alignment is not very high due to the relatively high beam temperature.

IV. COMPARISON WITH EXPERIMENTAL RESULTS

To allow a comparison with the experimental results from Ref. [15], the numerical results for $p^{2+}_{a,b}(\theta)$ and $p^{+}_{a}(\theta)$ ($a,b = \pi,\sigma$) were convolved with $f(\theta,\tau)$ to give a normalized yield $Y_{a,b}(\tau)$ as a function of delay time τ:

$$Y_{a,b}(\tau) = \frac{\int d\theta f(\theta,\tau)\,p^{2+}_{a,b}(\theta)}{\int dt\int d\theta f(\theta,\tau)\,p^{2+}_{a,b}(\theta)}, \quad (8)$$

where f is given by Eq. (7) and $p^{2+}_{a,b}$ (and p^{+}_{a} for the cationic case) are given by Eqs. (5) and (4). This convolution is valid since the rotational dynamics proceeds on much longer time scales than the ionization event(s). During the interaction with the short probe pulse (5 fs), rotational dynamics is frozen.

Since the nondissociative states can be accessed by ionization from two π_u orbitals, $Y_{\pi,\pi}(\tau)$ describes, according to our model, the yield of $C_2H_2^{2+}$. The yield of $C_2H_2^{+}$ is described by $Y_{\pi}(\tau)$. The sum of $Y_{\pi,\sigma}$ and $Y_{\sigma,\pi}$ describes the population of the dissociative $^3\Pi_u$ state and hence the dicationic fragment yield into $C_2H^+ + H^+$, $CH^+ + CH^+$, and $CH_2^+ + C^+$.

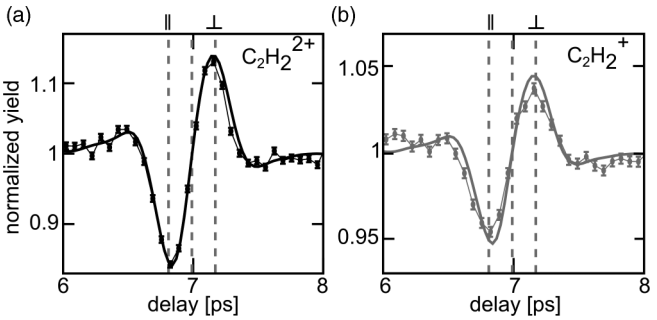

FIG. 13. Comparison of the theoretically predicted delay-dependent yield with experimental results [15]. Left, $C_2H_2^{2+}$ vs $Y_{\pi,\pi}$; right, $C_2H_2^{+}$ vs Y_{π}. For other symbols see Fig. 12.

In Fig. 13, we compare the calculated yields of Y_{π} and $Y_{\pi,\pi}$ with the experimentally measured yield [15] of $C_2H_2^{+}$ and $C_2H_2^{2+}$ around the half revival of the rotational wave packet at delay times between 6 and 8 ps. The yields were normalized such that the yield is equal to 1 for the randomly aligned sample. For the yield of the ionic and dicationic species, the qualitative and quantitative agreement is excellent.

In Fig. 14, a similar comparison is shown for $Y_{\pi,\sigma}$ and $Y_{\sigma,\pi}$ with the experimentally measured fragmentation yields. Good agreement is found for the hydrogen migration channel

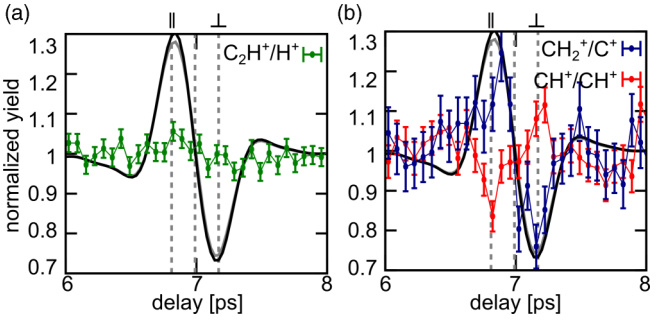

FIG. 14. Comparison of $Y_{\pi,\sigma}$ (black line) and $Y_{\sigma,\pi}$ (gray line) with experimental results [15] (dots with error bars, connected by thin lines) of fragmentation yields (a) for $C_2H^+ + H^+$ and (b) for $CH^+ + CH^+$ and $CH_2^+ + C^+$.

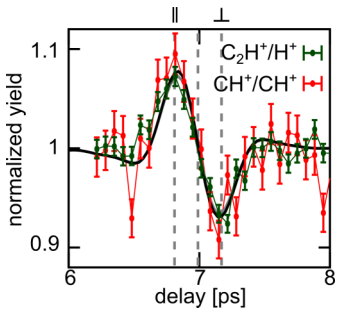

FIG. 15. Comparison of $Y^{\mathrm{circ}}_{\pi,\sigma}$ (black line) and $Y^{\mathrm{circ}}_{\sigma_\pi}$ (gray line) with experimental results of fragmentation yields in circularly polarized light.

[blue (dark gray) dots in Fig. 14(b)]. However, for $C_2H^+ + H^+$ [dark green (gray) dots in Fig. 14(a)] and $CH^+ + CH^+$ [red (light gray) dots in Fig. 14(b)], the predicted yield does not agree with the experimental values. This suggests that the present model, which captures only sequential ionization into one final state, is insufficient for the description of some of the experimental results and that, hence, the model is missing some relevant physical processes. Possible processes are nonsequential ionization, excitation, or ionization to even higher lying electronic states.

To shed some light onto the missing processes, we apply our model to experimental results obtained in circularly polarized light. Here, no prominent alignment dependence of excitation can be expected. Furthermore, nonsequential ionization and recollisional excitation are also excluded in circularly polarized light fields. To this end, the yields $Y^{\mathrm{circ}}_{\pi,\sigma}$ and $Y^{\mathrm{circ}}_{\sigma,\pi}$ are calculated from

$$Y^{\mathrm{circ}}_{a,b}(\tau) = \frac{\left\langle \int d\theta\, f(\theta,\tau)\, p^{2+}_{a,b}(\alpha(\theta)) \right\rangle}{\int d\tau \left\langle \int d\theta\, f(\theta,\tau)\, p^{2+}_{a,b}(\alpha(\theta)) \right\rangle}, \tag{9}$$

where

$$\cos(\alpha(\theta)) = \cos(\beta)\sin(\gamma)\sin(\theta) + \sin(\beta)\cos(\theta), \tag{10}$$

and $a,b = \pi,\sigma$. The average value, denoted by the angle brackets, is taken over the angles β and γ. The angle β thereby describes the instantaneous polarization of $\mathbf{E}(t)$. The angle γ is the azimuthal angle of the molecular axis relative to the polarization plane of the laser.

As shown in Fig. 15, the model correctly reproduces the results in circularly polarized light even for the $CH^+ + CH^+$ and $C_2H^+ + H^+$ channels. The excellent agreement between the model and the experiment for circularly polarized light suggests that in linearly polarized fields discussed above (Fig. 14), recollisional or possibly excitation processes play an important role for those reaction pathways.

This is also suggested when considering the kinetic energy release (KER) distributions. The KER distribution of the $C_2H^+ + H^+$ reaction channel exhibits a double-peak structure in linearly polarized light as shown in Fig. 16.

In circularly polarized light, the high KER peak around 5 eV is suppressed, suggesting the dominance of recollisional ionization in the high-KER regime. The low KER peak around 3.5 eV, on the other hand, remains visible even in circularly polarized light, suggesting contributions from

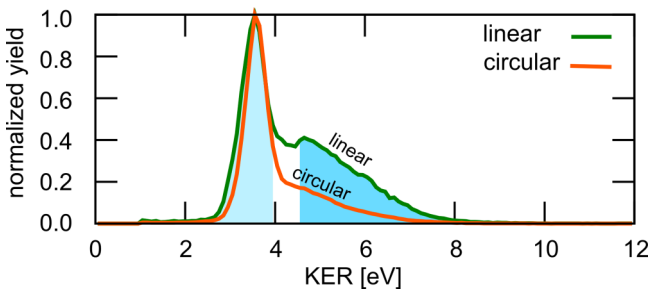

FIG. 16. Experimentally measured KER distribution for the $C_2H^+ + H^+$ channel for linearly and circularly polarized light.

sequential ionization. Comparing the model predictions for $C_2H^+ + H^+$ in linearly polarized light with the experimental results for KER $\leqslant$ 4 eV, good agreement between the model and the experiment can be achieved (see Fig. 17). This suggests that the low KER peak results indeed predominantly from sequential ionization and only a weak influence from other ionization mechanisms is implied.

The experimental results for KER $\geqslant$ 4.5 eV (not shown), on the other hand, show an opposing trend with a lower fragmentation yield for parallel alignment and a higher fragmentation yield for orthogonal alignment.

V. PROCESSES BEYOND THE PRESENT MODEL

The model as described so far neglects two processes which are potentially important in molecule-field interactions: field-excitation and recollisional processes. In the following we address these effects.

A. Recollision

The importance of recollisional processes to the strong-field fragmentation of acetylene has been discussed above. Theoretical modeling of recollisional ionization remains a challenge due to the necessary treatment of several electrons and the large excursion lengths of the electrons that have to be taken into account. While the probability for the primary electron to return to the core has been shown to depend on the orbital shape and the molecular alignment [49–52], probability for recollisional ionization itself has not been studied so far. The one-electron - two-electron process happening in the presence of a strong field at a molecule

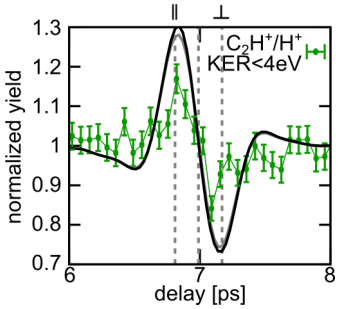

FIG. 17. Same as Fig. 14(b), but experimental values for $C_2H^+ + H^+$ fragments with low KER (< 4 eV) only.

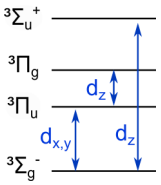

FIG. 18. States and dipole transition elements included in the dynamics calculation.

is very difficult to describe due to the comparatively low impact energy of the returning electron. However, we have shown in the last section that recollisional processes—while unimportant for circularly polarized light and for the low KER peak of the $C_2H^+ + H^+$ fragmentation—are important for some fragmentation reactions in acetylene, which necessitates further studies.

B. Field excitation

Field-driven dipole transitions in the neutral and in the singly ionic and dicationic manifolds can lead to population of excited electronic states. Thereby, the field-excitation probability depends on the molecular alignment relative to the laser polarization direction.

The energy gaps to the first excited dipole-coupled state in the Franck-Condon region are similar in the neutral molecule, the cation, and the dication. It is therefore reasonable to assume that the average probability for field excitation is similar in all three cases. Therefore, only the field-driven dynamics on the dicationic triplet manifold is studied in the following.

We simulate the wave-packet dynamics in reduced dimensions assuming Born-Oppenheimer dynamics. The propagation is performed on a grid using the split-operator method. Due to the much longer vibrational period of the C-C bond, only the much faster C-H stretching modes are considered in the following simulation. Furthermore, only the lowest-lying and strongly dipole coupled triplet states, the $^3\Sigma_g^-$ ground state, the first and second excited triplet states ($^3\Pi_u$ and $^3\Pi_g$), and the first $^3\Sigma_u^-$ state are taken into account. Dipole couplings are considered between $^3\Sigma_g^-$ and $^3\Pi_u$, between $^3\Sigma_g^-$ and $^3\Sigma_u^-$, and between $^3\Pi_u$ and $^3\Pi_g$ (see Fig. 18). The corresponding electronic states and transition dipoles were calculated using a state-averaged CAS-SCF(8,8) calculation with subsequent multireference configuration-interaction calculation. The initial wave packet was chosen to start in a dicationic dressed state, with the width corresponding to the wave packet in the neutral ground state, thus mimicking a Franck-Condon wave packet. The laser intensity was set to 4×10^{14} W/cm^2 with a FWHM duration of 4.5 fs.

Figure 19 shows exemplarily the population dynamics for the excited states assuming a CEP of 0°, a relative laser polarization axis of $\theta = 45°$, and the moment of ionization to the dicationic manifold 0.5 fs after the maximum of the field envelope.

Figure 20 shows the resulting fragmentation probability as a function of the instant of ionization (i.e., the instant in time when the dicationic manifold is reached) for three different alignment angles θ of the molecule relative to the laser polarization axis for a CEP of 0° (cos pulse). Similar results were obtained for other CEPs.

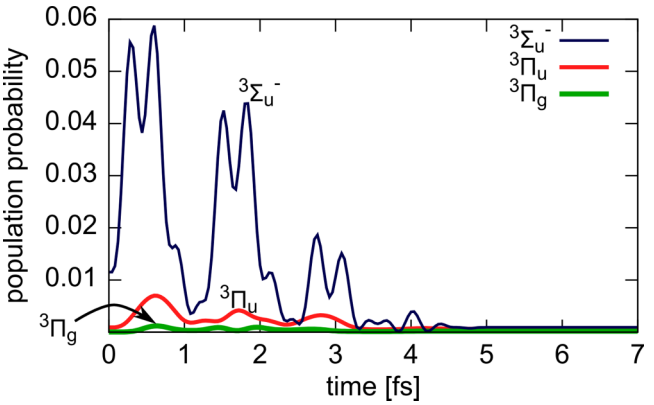

FIG. 19. Population dynamics for the excited states assuming CEP = 0°, $\theta = 45°$, and the moment of ionization to the dicationic manifold 0.5 fs after the maximum of the field envelope.

Not surprisingly, the excitation probability depends on the molecular alignment relative to the laser polarization. Interestingly, however, the alignment angle leading to the strongest fragmentation depends on the moment of ionization: the probability for field-excitation-induced fragmentation is larger for parallel alignment than for perpendicular alignment, if ionization happens at $t \approx 0.6$ fs, corresponding to a zero electric field, where the probability for recollisional ionization is high. At the field maximum ($t = 0$ fs), when the probability for sequential ionization is highest, the fragmentation probability is higher for perpendicular alignment. However, overall, the calculated excitation probability is small ($< 0.3\%$). If it were field-driven dipole transitions, which are mainly responsible for the fragmentation process and not ionization from lower-lying orbitals and recollisions, then the overall fragmentation probability would have to be below 0.3% as well. Since the experimentally observed fragmentation probabilities are significantly higher (in the region of several percent), we can

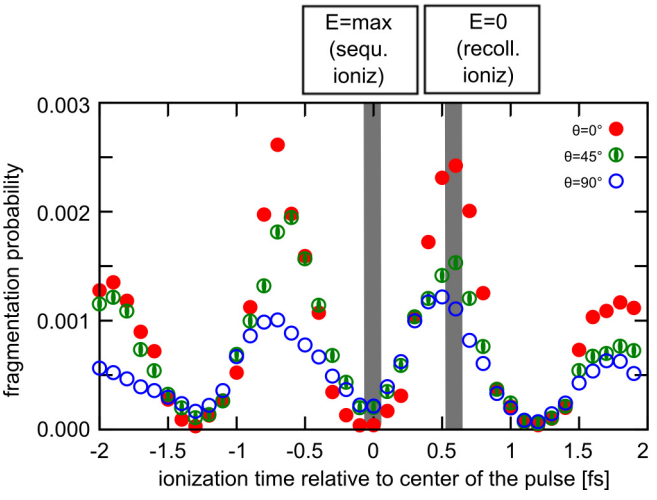

FIG. 20. Calculated fragmentation probability as a function of the moment of double ionization and the alignment angle. Time $t = 0$ fs corresponds to the center of the pulse with CEP = 0°.

conclude that although field-excitation processes will depend strongly on the molecular alignment, it is a good approximation to neglect these effects in the current model due to their small influence.

VI. SUMMARY AND CONCLUSION

In summary, we have presented theoretical approaches describing the complex strong-field-driven molecular dynamics leading to the experimentally observed alignment-dependent fragmentation of small molecules in an intense, few-cycle laser field. We have compared two conceptually different approaches calculating the ionization yield of acetylene at different angles relative to the polarization axis of the laser pulse: one using TD-DFT methods, and a second one based on a Dyson orbital approach. Despite the different approximations implied in both methods, we have obtained almost identical results. Our model is based on sequential double ionization which, together with wave-packet calculations for the rotational dynamics, is very successful in describing the experimental results of Ref. [15]. For many of the experimentally observed reaction channels, the alignment-dependent fragmentation patterns could be reproduced quantitatively within our model. For two channels, namely, $C_2H^+ + H^+$ and $CH^+ + CH^+$, based on our theoretical investigations we conclude that electron recollision plays an important role. Field-driven population transfer was shown to play a minor role in the overall dynamics. Understanding of the processes underlying the fragmentations is essential in allowing predictions for other systems. Our results stimulate further investigation on the influence of recollisional processes in strong-field-driven molecular dynamics.

ACKNOWLEDGMENTS

K.D.D. acknowledges helpful discussions with Dr. A. Saenz and funding from the International Max-Planck Research School for Advanced Photon Science (IMPRS-APS). Funding from the Austrian Science Fund (FWF) under Grants No. P21463-N22, No. P27491-N27, No. P28475-N27, and No. SFB F4903-N23 (NextLite) is acknowledged.

[1] M. F. Kling, C. Siedschlag, A. J. Verhoef, J. I. Khan, M. Schultze, T. Uphues, Y. Ni, M. Uiberacker, M. Drescher, F. Krausz *et al.*, Science **312**, 246 (2006).
[2] X. Xie, K. Doblhoff-Dier, S. Roither, M. S. Schöffler, D. Kartashov, H. Xu, T. Rathje, G. G. Paulus, A. Baltuška, S. Gräfe *et al.*, Phys. Rev. Lett. **109**, 243001 (2012).
[3] A. Jaron-Becker, IEEE J. Sel. Top. Quantum Electron. **18**, 105 (2012).
[4] J. L. Hansen, L. Holmegaard, J. H. Nielsen, H. Stapelfeldt, D. Dimitrovski, and L. B. Madsen, J. Phys. B: At. Mol. Phys. **45**, 015101 (2012).
[5] T. K. Kjeldsen, C. Z. Bisgaard, L. B. Madsen, and H. Stapelfeldt, Phys. Rev. A **71**, 013418 (2005).
[6] M. Spanner and S. Patchkovskii, Phys. Rev. A **80**, 063411 (2009).
[7] P. von den Hoff, I. Znakovskaya, S. Zherebtsov, M. F. Kling, and R. Vivie-Riedle, Appl. Phys. B **98**, 659 (2010).
[8] S. Petretti, Y. V. Vanne, A. Saenz, A. Castro, and P. Decleva, Phys. Rev. Lett. **104**, 223001 (2010)
[9] S. Petretti, A. Saenz, A. Castro, and P. Decleva, Chem. Phys. **414**, 45 (2013).
[10] R. de Nalda, E. Heesel, M. Lein, N. Hay, R. Velotta, E. Springate, M. Castillejo, and J. P. Marangos, Phys. Rev. A **69**, 031804 (2004).
[11] R. Velotta, N. Hay, M. B. Mason, M. Castillejo, and J. P. Marangos, Phys. Rev. Lett. **87**, 183901 (2001).
[12] X. X. Zhou, X. M. Tong, Z. X. Zhao, and C. D. Lin, Phys. Rev. A **71**, 061801(R) (2005).
[13] J. Itatani, J. Levesque, D. Zeidler, H. Niikura, H. Pepin, J. C. Kieffer, P. B. Corkum, and D. M. Villeneuve, Nature (London) **432**, 867 (2004).
[14] C. Vozzi, M. Negro, F. Calegari, G. Sansone, M. Nisoli, S. D. Silvestri, and S. Stagira, Nat. Phys. **7**, 822 (2011).
[15] X. Xie, K. Doblhoff-Dier, H. Xu, S. Roither, M. S. Schöffler, D. Kartashov, S. Erattupuzha, T. Rathje, G. G. Paulus, K. Yamanouchi *et al.*, Phys. Rev. Lett. **112**, 163003 (2014).
[16] MOLCAS webpage, http://www.molcas.org
[17] P. Plessis and P. Marmet, Int. J. Mass Spectrom. Ion Processes **70**, 23 (1986).
[18] M. Peric, B. Engels, and M. Hanrath, Chem. Phys. **238**, 33 (1998).
[19] M. Peric and B. Engels, Chem. Phys. **238**, 47 (1998).
[20] E. M. L. Ohrendorf, F. Tarantelli, and L. S. Cederbaum, J. Chem. Phys. **92**, 2984 (1990).
[21] R. Thissen, J. Delwiche, J. M. Robbe, D. Duflot, J. P. Flament, and J. H. D. Eland, J. Chem. Phys. **99**, 6590 (1993).
[22] T. S. Zyubina, Y. A. Dyakov, S. H. Lin, A. D. Bandrauk, and A. M. Mebel, J. Chem. Phys. **123**, 134320 (2005).
[23] H. Akagi, T. Otobe, A. Staudte, A. Shiner, F. Turner, R. Drner, D. Villneuve, and P. Corkum, Science **325**, 1364 (2009).
[24] O. Smirnova, Y. Mairesse, S. Patchkovskii, N. Dudovich, D. Villeneuve, P. B. Corkum, and M. Y. Ivanov, Nature (London) **460**, 972 (2009).
[25] J. P. Farrell, S. Petretti, J. Förster, B. K. McFarland, L. S. Spector, Y. V. Vanne, P. Decleva, P. H. Bucksbaum, A. Saenz, and M. Gühr, Phys. Rev. Lett. **107**, 083001 (2011).
[26] D. N. Fittinghoff, P. R. Bolton, B. Chang, and K. C. Kulander, Phys. Rev. Lett. **69**, 2642 (1992).
[27] P. B. Corkum, Phys. Rev. Lett. **71**, 1994 (1993).
[28] C. Cornaggia and P. Hering, Phys. Rev. A **62**, 023403 (2000).
[29] L. Keldysh, Sov. Phys. JETP **20**, 1307 (1965).
[30] A. M. Perelomov, V. S. Popov, and M. V. Terent'ev, Sov. Phys. JETP **23**, 924 (1966).
[31] F. H. M. Faisal, J. Phys. B: At. Mol. Phys. **6**, L89 (1973).
[32] H. R. Reiss, Phys. Rev. A **22**, 1786 (1980).
[33] N. B. Delone and V. P. Krainov, J. Opt. Soc. Am. B **8**, 1207 (1991).

[34] X. M. Tong, Z. X. Zhao, and C. D. Lin, Phys. Rev. A **66**, 033402 (2002).
[35] X. Andrade, J. Alberdi-Rodriguez, D. A. Strubbe, M. J. T. Oliveira, F. Nogueira, A. Castro, J. Muguerza, A. Arruabarrena, S. G. Louie, A. Aspuru-Guzik *et al.*, J. Phys.: Condens. Matter **24**, 233202 (2012).
[36] A. Casto, H. Appel, M. Oliveira, C. A. Rozzi, X. Andrade, F. Lorenzen, M. A. L. Marques, E. K. U. Gross, and A. Rubio, Phys. Status Solidi B **243**, 2465 (2006).
[37] M. A. L. Marques, A. Castro, G. F. Bertsha, and A. Rubio, Comput. Phys. Commun. **151**, 60 (2003).
[38] J. P. Perdew and A. Zunger, J. Phys. B: At. Mol. Phys. **23**, 5048 (1981).
[39] R. van Leeuwen and E. J. Baerends, Phys. Rev. A **49**, 2421 (1994).
[40] A. Crawford-Uranga, U. De Giovannini, E. Räsänen, M. J. T. Oliveira, D. J. Mowbray, G. M. Nikolopoulos, E. T. Karamatskos, D. Markellos, P. Lambropoulos, S. Kurth *et al.*, Phys. Rev. A **90**, 033412 (2014).
[41] P. R. T. Schipper, O. V. Gritsenko, S. J. A. van Gisbergen, and E. J. Baerdens, J. Chem. Phys. **112**, 1344 (2000).
[42] A. S. Alnaser, M. Kübel, R. Siemering, B. Bergues, N. G. Kling, K. J. Betsch, Y. Deng, J. Schmidt, Z. A. Alahmed, A. M. Azzeer *et al.*, Nat. Commun. **5**, 3800 (2014).
[43] M. Musia and R. J. Bartlett, Chem. Phys. Lett. **384**, 210 (2004).
[44] R. Murray, M. Spanner, S. Patchkovskii, and M. Y. Ivanov, Phys. Rev. Lett. **106**, 173001 (2011).
[45] R. Murray, W.-K. Liu, and M. Y. Ivanov, Phys. Rev. A **81**, 023413 (2010).
[46] J. Ortigoso, M. Rodriguez, M. Gupta, and B. Friedrich, J. Chem. Phys. **110**, 3870 (1999).
[47] M. Swart, P. Th. van Duijnen, and J. G. Snijders, J. Mol. Struc. **458**, 11 (1998).
[48] National Institute of Standards and Technology, http://cccbdb.nist.gov/exp2.asp?casno=74862
[49] V. R. Bhardwaj, D. M. Rayner, D. M. Villeneuve, and P. B. Corkum, Phys. Rev. Lett. **87**, 253003 (2001).
[50] M. Lein, J. Phys. B: At. Mol. Phys. **36**, L155 (2003).
[51] X. Y. Jia, W. D. Li, J. Fan, J. Liu, and J. Chen, Phys. Rev. A **77**, 063407 (2008).
[52] S. Weber, M. Oppermann, M. Ivanov, and J. Marangos, J. Mod. Opt. **60**, 1379 (2013).